

## Article

# Carbonaceous Fe<sub>x</sub>P Synthesized via Carbothermic Reduction of Dephosphorization Slag as Hydrogen Evolution Catalyst for Water Splitting

Sai He <sup>1</sup>, Yaqin Liu <sup>1</sup>, Shanlong Peng <sup>2,\*</sup> and Lu Lin <sup>1,\*</sup>

<sup>1</sup> Metallurgical Technology Research Institute, Central Iron and Steel Research Institute, Beijing 100081, China; hesai1011@163.com (S.H.); liuyaqin7777@163.com (Y.L.)

<sup>2</sup> Department of Metallurgical and Ecological Engineering, University of Science and Technology Beijing, Beijing 100083, China

\* Correspondence: g20198284@xs.ustb.edu.cn (S.P.); linlu\_luke@sina.com (L.L.)

**Abstract:** Developing the high-efficiency and cheap non-noble catalysts towards hydrogen evolution reaction (HER) is of significance for water splitting. Herein, for the first time, we report a simple method of acid leaching combined with carbothermic reduction with dephosphorization slag to construct a carbonaceous Fe<sub>x</sub>P/C catalyst. In alkaline medium, the corresponding overpotential when the output current density was 10 mA cm<sup>-2</sup> ( $\eta_{10}$ ) was only 145 mV. Additionally, there was no obvious attenuation after 3000 cycles, which showed significantly better activity and stability than that of non-carbonaceous Fe<sub>x</sub>P catalysts prepared by gas–solid phosphating. The structure and composition of Fe<sub>x</sub>P/C were characterized by X-ray diffraction, scanning electron microscope, energy dispersive spectroscopy, and inductively coupled plasma atomic emission spectrometer. The electrochemical properties of the electrode were evaluated by cyclic voltammetry, linear scanning voltammetry, electrochemical impedance spectroscopy, and cyclic stability. The results showed that the prepared Fe<sub>x</sub>P/C was composed of FeP-Fe<sub>2</sub>P mixed nanocrystals supported on amorphous carbon. Compared with Fe<sub>x</sub>P, the synergistic catalysis of the FeP and Fe<sub>2</sub>P phases as well as the interactive support effect between the FeP-Fe<sub>2</sub>P mixed nanocrystals and the amorphous carbon support will attribute the rich active sites for electrocatalytic reaction and reduce the charge transfer resistance. Thus, Fe<sub>x</sub>P/C has good hydrogen evolution activity and stability. Overall, the preparation of catalysts with high additional value based on dephosphorization slag was preliminarily explored.

**Keywords:** water splitting; hydrogen evolution reaction; transition metal phosphides; iron phosphide



**Citation:** He, S.; Liu, Y.; Peng, S.; Lin, L. Carbonaceous Fe<sub>x</sub>P Synthesized via Carbothermic Reduction of Dephosphorization Slag as Hydrogen Evolution Catalyst for Water Splitting. *Inorganics* **2022**, *10*, 70. <https://doi.org/10.3390/inorganics10060070>

Academic Editor: Francis Verpoort

Received: 30 April 2022

Accepted: 23 May 2022

Published: 26 May 2022

**Publisher's Note:** MDPI stays neutral with regard to jurisdictional claims in published maps and institutional affiliations.



**Copyright:** © 2022 by the authors. Licensee MDPI, Basel, Switzerland. This article is an open access article distributed under the terms and conditions of the Creative Commons Attribution (CC BY) license (<https://creativecommons.org/licenses/by/4.0/>).

## 1. Introduction

The use of fossil fuels has caused a series of environmental pollution problems. Developing clean, efficient, and sustainable energy can effectively solve this problem and is also the key to promoting carbon neutralization [1,2]. Hydrogen is considered the ideal choice of energy in the future. Water electrolysis via renewable powers, e.g., solar power and wind power, can produce clean hydrogen without carbon emission, which has great development potential [3,4]. At present, the precious metals Pt, Ir, and Ru and their compounds are the most excellent electrocatalysts for hydrogen and oxygen production [2,5]. However, the high cost and scarcity of these precious metals seriously hinder their large-scale application. Therefore, the research and development of non-noble metal-based electrocatalysts with high abundance, low cost, and high activity have attracted extensive attention. In recent years, transition metals (Fe, Co, Ni, etc.) and their compounds have gradually become a research hotspot because of their low price, controllable morphology, and excellent properties in electrocatalysis [6,7]. Transition metal phosphides (TMPs) have always been used as catalysts for hydrogenation reactions, especially hydrodesulfurization reactions. Recently,

TMPs were widely used by researchers as catalysts for hydrogen evolution reaction (HER), which shows its excellent catalytic performance [8,9].

Iron is the most abundant metal element on Earth. Iron phosphide ( $\text{Fe}_x\text{P}$ ) is a metal-rich TMP. It is a good conductor of heat and electricity, and also has very high thermal and chemical stability. Recently, new studies have shown that  $\text{Fe}_x\text{P}$ -based catalysts have very good catalytic activity for HER.  $\text{Fe}_x\text{P}$  has been regarded as a good catalytic material that can replace Pt/C [10]. Generally, it is accepted that the catalytic site origin from the coordinated P and Ni atoms leads to a lower barrier for the rate-limiting HER step since the Gibbs free energy of the P atom (as the active site) is near zero. Moreover, the carbon substrate is also more conducive to electron transfer, which makes the  $\text{Fe}_x\text{P}$  composite have good catalytic properties. Unfortunately, despite extensive research and development on the catalytic activity and stability of these transition metal phosphides, their HER properties have, so far, struggled to meet the requirements of industrial hydrogen production [11,12]. In order to obtain better-performing catalysts to meet the requirements of large-scale hydrogen manufacturing, it is particularly important to optimize the material design of  $\text{Fe}_x\text{P}$  and deepen the understanding of the relationship between the structure and properties of such materials [13].

So far, the atomic and electrical properties of  $\text{Fe}_x\text{P}$  have been regulated by interface regulation and nanostructure synthesis [14,15]. For example,  $\text{Fe}_x\text{P}$  nanowire materials with large specific areas have been successfully synthesized. Based on the analysis results of XPS, it is considered that the unsaturated coordination center Fe and P atoms are the active centers of HER and they work together. It is also possible to improve the performance of  $\text{Fe}_x\text{P}$  by coating  $\text{Fe}_x\text{P}$  on the surface of Fe nanoparticles to form a core-shell structure, which effectively enhances the chemisorption process of hydrogen atoms on the  $\text{Fe}_x\text{P}$  surface [16]. On the other hand, the change of Gibbs free energy on the  $\text{Fe}_x\text{P}$  surface during HER is analyzed by density functional theory (DFT). It is found that, when a thin FeO layer is coated on the FeP surface, the absorption of  $\text{H} \cdot$  can be significantly reduced to improve HER catalytic activity of  $\text{Fe}_x\text{P}$  [15,17]. Otherwise, different phases are produced due to different phosphorus contents, such as FeP and  $\text{Fe}_2\text{P}$  [18]. As described above,  $\text{Fe}_x\text{P}$  with a higher phosphorus content can have more active sites to capture protons and improve corrosion resistance to benefit HER [19]. However, with the increase of phosphorus content, phosphorus atoms will greatly limit the electron delocalization (free electrons) of metal atoms, thus hindering the conductivity and weakening HER activity. Therefore, it is necessary to explore a balanced phosphorus content. It is speculated that higher phosphorus content will always lead to higher HER activity and better stability without seriously reducing the conductivity of  $\text{Fe}_x\text{P}$ . Additionally, using carbon materials such as carbon nanotubes (CNTs), graphite, graphene, and porous carbon as support of TMPs can not only make them have a huge surface area but also improve the conductivity of hybrid catalysts [11,20]. Moreover, the coupled carbon material can also adjust the electron density and potential distribution in the hybrid material, which will improve the activity and stability of the catalysts. In short, the catalyst compounded with carbon materials can make full use of the excellent conductivity and good dispersion of carbon materials and is conducive to improving the electrocatalytic activity.

Generally, the  $\text{Fe}_x\text{P}$  is prepared from an iron salt solution and phosphoric acid by a liquid-phase precipitation method. This method has the advantages of a simple process, high purity, and good crystal form, but the production cost is high. The dephosphorization slag produced in the iron and steel industry is mainly a mixture of phosphorus and iron. In addition, it also includes many beneficial element components, such as nickel, manganese, and sulfur. We tried to use dephosphorization slag as the raw material for the preparation of  $\text{Fe}_x\text{P}$  and constructed a carbonaceous  $\text{Fe}_x\text{P}$  electrocatalyst by combining the acid pickling and carbothermic reduction. The structure and composition of the prepared carbonaceous  $\text{Fe}_x\text{P}$  electrocatalyst as well as the non-carbonaceous  $\text{Fe}_x\text{P}$  were characterized, and the performance of the hydrogen production by electrolyzing water in an alkaline solution was further studied.

## 2. Materials and Methods

### 2.1. Preparation of Electrocatalysts

Firstly, the dephosphorization slags were ball-milled and dispersed in the mixed acidic solution (sulfuric acid,  $1.5 \text{ mol L}^{-1}$  and nitric acid,  $1.5 \text{ mol L}^{-1}$ , total volume of 500 mL, volume ratio = 1:1). The fine, dephosphorization slag particles were digested and a final red leaching solution was obtained. Then, the ammonia solutions were dropped into the leaching solution to produce a mixture precipitation consisting of phosphorus and iron. The mixture precipitation was further filtrated and dried. Finally, the dried mixture precipitation was added with excess carbon powder, ground, mixed evenly, put into the crucible, and calcined in an Ar atmosphere furnace at  $1200 \text{ }^\circ\text{C}$  for 2 h to obtain  $\text{Fe}_x\text{P}/\text{C}$ .

As for the preparation of  $\text{Fe}_x\text{P}$ , the porcelain boat filled with the  $\text{NaH}_2\text{PO}_2$  powder (250 mg) was placed in the heating zone of the quartz tube, and another porcelain boat containing the mixture precipitation samples was placed on the stove downstream. The sample was then heated to  $350 \text{ }^\circ\text{C}$  in an Ar atmosphere and incubated for 2 h. After cooling to room temperature,  $\text{Fe}_x\text{P}$  was obtained [14].

### 2.2. Physical and Chemical Characterization

The samples were analyzed by field emission scanning electron microscope (SEM, hitachi-sub010) and energy dispersive spectroscopy (EDS). Powder X-ray diffraction (XRD) spectra were recorded on a RIGAKU D/max 2200 PC diffractometer with a graphite monochromator and Cu KCT radiation source ( $\lambda = 0.15418 \text{ nm}$ ). The composition of metal elements was tested by an inductively coupled plasma atomic emission spectrometer (ICP-AES).

### 2.3. Electrochemical Characterization

All electrochemical tests were carried out on a VMP2 electrochemical workstation (Bio-logic, France) using a standard three-electrode system, and the electrolyte was 1 M KOH. For the working electrode, 5 mg of catalyst powder was dispersed in 1 mL isopropyl alcohol, to which 50  $\mu\text{L}$  of Nafion<sup>®</sup> solution (5 wt%, Dupont) was added. The mixture was then homogenized for 1 h in an ice ultrasonic bath to form an ink. Based on the ICP results, the nominal loading of the active phase ( $\text{Fe}_x\text{P}$ ) on the testing electrodes was controlled to be the same by adjusting the amount of the pipetting inks on a graphite carbon substrate with a geometric area of  $0.5 \text{ cm}^2$  and was dried at  $75 \text{ }^\circ\text{C}$  in a vacuum oven. For the  $\text{Fe}_x\text{P}$  and  $\text{Fe}_x\text{P}/\text{C}$ , the nominal loading of  $\text{Fe}_x\text{P}$  was  $0.2 \text{ mg cm}^{-2}$ ; for the Pt/C, the nominal loading of Pt was  $0.05 \text{ mg cm}^{-2}$ . These testing electrodes were used as working electrodes for the electrochemical measurement. Considering that the dissolution of the Pt in an alkaline electrolyte will affect the test of HER, the graphite carbon rod and Hg/HgO electrode were selected as a counter electrode and reference electrode, respectively. All potentials collected by the Hg/HgO reference electrode were converted to potential with respect to the reversible hydrogen electrode with the following formula,  $E(\text{RHE}) = E(\text{Hg}/\text{HgO}) + 0.0591 \times \text{pH} + 0.098$ , and converted to the potential relative to the reversible hydrogen electrode (RHE).

The working electrode was initially pretreated electrochemically by 10 cycles of cyclic voltammetry scanning (0 and 1.1 V at  $100 \text{ mV s}^{-1}$ ). CVs were then recorded in the potential range of  $-0.1$  to  $0.1 \text{ V}$  at different scan rates of 20 to  $120 \text{ mV s}^{-1}$  for 10 cycles. A stable cycle (the 10th cycle) of the CVs was used for calculating the electrochemical surface area (ECSA). The polarization curve was measured by linear scanning voltammetry (LSV) in the potential range of 0.1 to  $-0.4 \text{ V}$ , and the scanning speed was  $5 \text{ mV s}^{-1}$ . All results obtained were  $iR$  corrected, and the internal resistance and contact resistance of the solution were deducted. Electrochemical impedance spectroscopy was performed at an open circuit voltage with an amplitude of 5 mV in the frequency range of 100,000 Hz to 0.1 Hz. An accelerated life test was carried out by potential cycling in the potential range of 0.1 to  $-0.4 \text{ V}$  at a scan rate of  $50 \text{ mV s}^{-1}$ . After the HER cycling for 3000 cycles, LSV was recorded in the potential range of 0.1 to  $-0.4 \text{ V}$ , and the scanning speed was  $5 \text{ mV s}^{-1}$ .

### 3. Results

The industrial dephosphorization slags were firstly treated by acid leaching and precipitation. The mixture precipitation precursor was then gas–solid phosphated with sodium hypophosphite under low temperature (the produced catalyst was  $\text{Fe}_x\text{P}$ ) and carbothermally reduced under high temperature (the produced catalyst is  $\text{Fe}_x\text{P}/\text{C}$ ). As shown in Figure 1, it was seen that the ball-milled dephosphorization slags were irregularly granular and the grain size was 10~80  $\mu\text{m}$ . It can be seen from the corresponding EDS spectrum that the main element composition of industrial dephosphorization slags was mainly Fe, P, C, etc. The further ICP analysis results are shown in Table 1. Both the ICP results together with the elemental weight% from the EDS data confirmed that the prepared catalysts were  $\text{Fe}_x\text{P}$  and carbonaceous  $\text{Fe}_x\text{P}/\text{C}$ . Compared with the  $\text{Fe}_x\text{P}$ , the Fe:P mass ratio of  $\text{Fe}_x\text{P}/\text{C}$  was decreased, and there was increased C content mainly due to the carbothermic reduction. For  $\text{Fe}_x\text{P}$ , it presented angular particles, which may be related to the structure of the precursor precipitated by acid precipitation. The low-temperature gas–solid phosphating treatment of sodium hypophosphite did not affect the microstructure of the precursor, and the particle size was between 100~400 nm. From the EDS data (shown in Figure 1e) and the EDS mapping image of the  $\text{Fe}_x\text{P}$  catalyst (shown in Figure 1b), it was seen that Fe and P elements were evenly distributed; so, it can be inferred that  $\text{Fe}_x\text{P}$  material was formed. For  $\text{Fe}_x\text{P}/\text{C}$ , due to the high-temperature carbothermic reduction treatment, it presented irregular, ellipsoidal particles, the bonding phase was generated between the grains, and the grain size was between 100~200 nm. From the EDS data (shown in Figure 1f), both the Fe, P, and C existed in the  $\text{Fe}_x\text{P}/\text{C}$ , and it can also be seen that the Fe and P elements were evenly distributed from the EDS mapping image of the  $\text{Fe}_x\text{P}/\text{C}$  catalyst (shown in Figure 1c). It can be inferred that the composite of  $\text{Fe}_x\text{P}$  and carbon was formed.

The XRD patterns of phosphating products prepared by different methods can be seen in Figure 2. As for  $\text{Fe}_x\text{P}$ , it was very consistent with  $\text{Fe}_3\text{P}$  (PDF#89-2712), and the obvious diffraction peaks were consistent with the crystal planes of  $\text{Fe}_3\text{P}$  [21,22], which can be related to the high mass ratio of Fe:P in  $\text{Fe}_x\text{P}$ . For  $\text{Fe}_x\text{P}/\text{C}$ , there were not only diffraction peaks consistent with the crystal plane of FeP (PDF#78-1443) but also diffraction peaks consistent with  $\text{Fe}_2\text{P}$  (PDF#51-0943), which corresponded to the crystal plane of  $\text{Fe}_2\text{P}$ , respectively, which indicated that the carbonaceous  $\text{Fe}_x\text{P}$  obtained by a high-temperature carbothermal reduction may be the mixed crystal structure of FeP and  $\text{Fe}_2\text{P}$  (FeP- $\text{Fe}_2\text{P}$  mixed nanocrystals) [18,23]. It should be noted that no obvious diffraction peak of graphitized carbon was observed. Although EDS showed the presence of carbon, the carbon may exist in the form of an amorphous phase. The above characterization and analysis confirmed that both the carbonaceous  $\text{Fe}_x\text{P}/\text{C}$  and non-carbonaceous  $\text{Fe}_x\text{P}$  were successfully prepared, but there were great differences in the microstructure, composition, and crystal phase structure, which may influence the electrocatalytic activities.

**Table 1.** ICP elemental analysis of  $\text{Fe}_x\text{P}$  and  $\text{Fe}_x\text{P}/\text{C}$ .

	C (Mass%)	Mn (Mass%)	P (Mass%)	Fe (Mass%)	Si (Mass%)	S (Mass%)
$\text{Fe}_x\text{P}$	0.02	0.56	14.53	84.74	0.21	0.01
$\text{Fe}_x\text{P}/\text{C}$	3.58	0.73	36.80	58.61	0.19	0.01

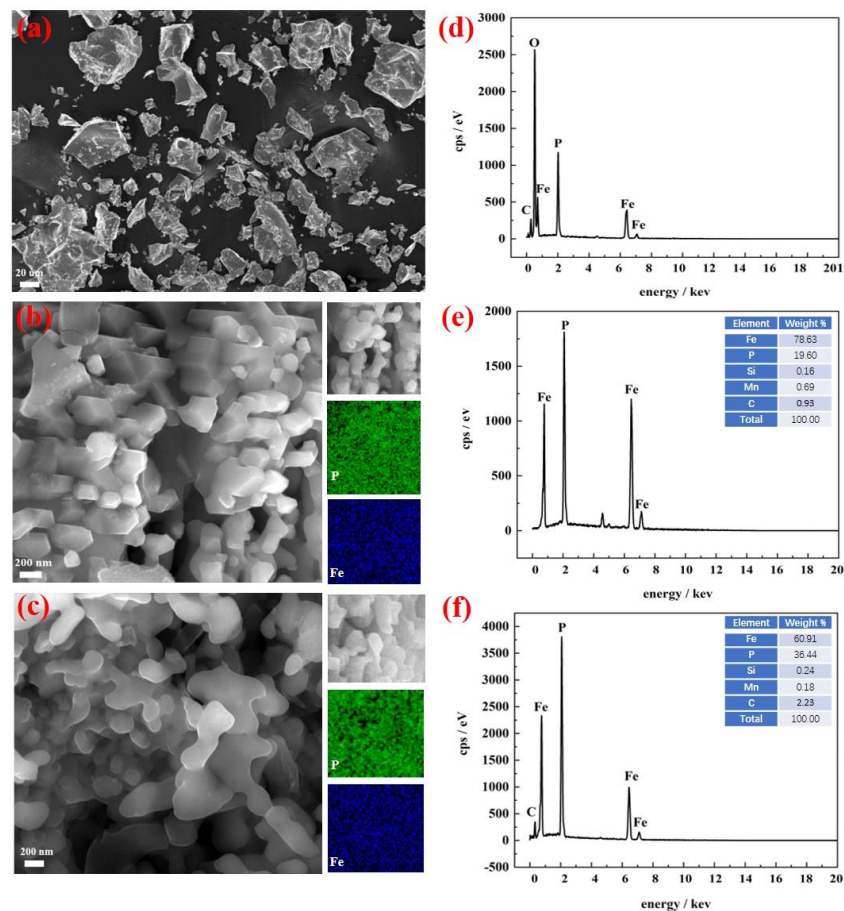


**Figure 1.** SEM image and corresponding EDS spectra of (a,d) dephosphorization slag, (b,e)  $\text{Fe}_x\text{P}$ , (c,f)  $\text{Fe}_x\text{P}/\text{C}$ . The inserts in (b,c) are selected SEM images and the corresponding elemental mapping images. The inserts in (e,f) are the corresponding elemental weight% from EDS data.

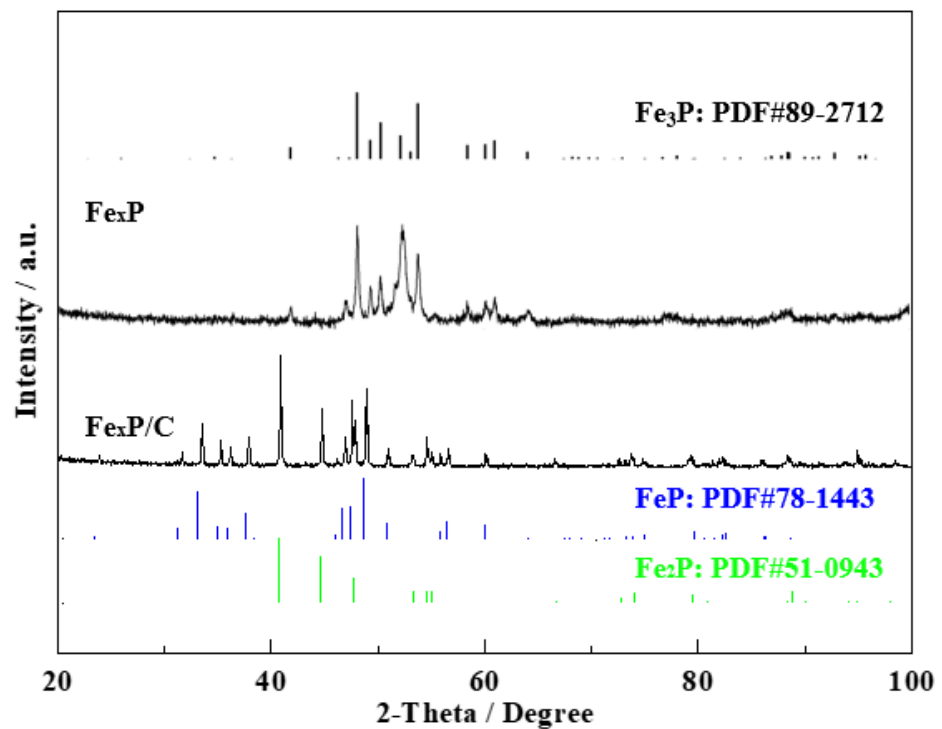


**Figure 2.** XRD pattern of  $\text{Fe}_x\text{P}$  and  $\text{Fe}_x\text{P}/\text{C}$ .

In order to explore the effects of catalysts on electrocatalytic activity due to different components, microstructure, and crystal structure,  $\text{Fe}_x\text{P}$ ,  $\text{Fe}_x\text{P}/\text{C}$ , and 20% Pt/C were loaded on a glassy carbon electrode and tested by linear sweep voltammetry (LSV). The obtained LSV curve and Tafel slope are shown in the Figure 3. In order to quantitatively compare the catalytic activities of different materials, two characteristics are usually mentioned. One is the onset overpotential ( $\eta_{\text{onset}}$ ), which is defined as the overpotential corresponding to the current density of  $0.5 \text{ mA cm}^{-2}$ . The other is the corresponding overpotential when the output current density of HER is  $10 \text{ mA cm}^{-2}$  ( $\eta_{10}$ ). An ideal catalyst can output a higher current density at a low overpotential. Among them, the commercial 20% Pt/C as the reference standard has the lowest overpotential ( $\eta_{\text{onset}} = 11 \text{ mV}$ ,  $\eta_{10} = 50 \text{ mV}$ , and the Tafel slope =  $43 \text{ mV dec}^{-1}$ ), showing extremely excellent HER activity, which also shows that the catalytic HER process of Pt/C materials follows the Volmer Tafel reaction mechanism, which is consistent with some reported literature [24,25].  $\text{Fe}_x\text{P}/\text{C}$  and carbon free  $\text{Fe}_x\text{P}$  show excellent HER activity, while  $\text{Fe}_x\text{P}/\text{C}$  ( $\eta_{\text{onset}} = 81 \text{ mV}$ ,  $\eta_{10} = 145 \text{ mV}$ ) has higher activity than  $\text{Fe}_x\text{P}$  ( $\eta_{\text{onset}} = 140 \text{ mV}$ ,  $\eta_{10} = 235 \text{ mV}$ ). It is inferred that both FeP and  $\text{Fe}_2\text{P}$  are active components for catalyzing HER. This may be due to the synergistic catalysis of FeP- $\text{Fe}_2\text{P}$  mixed nanocrystals, which make  $\text{Fe}_x\text{P}/\text{C}$  have better HER activity than  $\text{Fe}_x\text{P}$  ( $\text{Fe}_3\text{P}$  nanocrystalline structure). In addition, the carbonaceous phases also promote the improvement of HER activity, which may be attributed to the improvement of conductivity, dispersion, and interaction between the amorphous carbon support and FeP- $\text{Fe}_2\text{P}$  mixed nanocrystals. In addition, the Tafel slope reflects the kinetic characteristics of the material. When the Tafel slope is smaller, it shows that the better the kinetic properties of the material are, then the faster the reaction rate is.  $\text{Fe}_x\text{P}/\text{C}$  ( $45 \text{ mV dec}^{-1}$ ) showed a smaller Tafel slope than  $\text{Fe}_x\text{P}$  ( $56 \text{ mV dec}^{-1}$ ), indicating that  $\text{Fe}_x\text{P}/\text{C}$  had higher kinetic processes and improved HER activity. At the same time, the electrocatalytic HER process of the two materials followed the Volmer–Heyrovsky reaction mechanism [19,20].

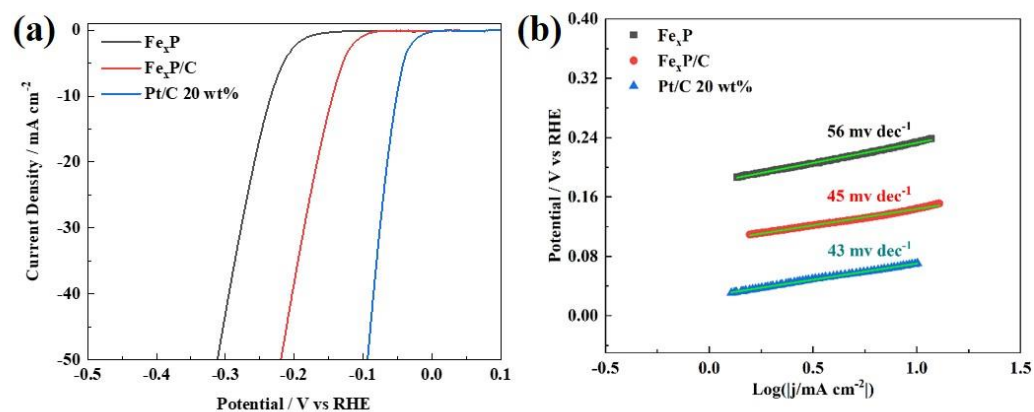


**Figure 3.** (a) LSV curves for 20 wt% Pt/C,  $\text{Fe}_x\text{P}$ , and  $\text{Fe}_x\text{P}/\text{C}$  in 1 M KOH; (b) the corresponding Tafel plot.

In order to understand the reason why  $\text{Fe}_x\text{P}/\text{C}$  has higher HER activity, EIS tests were carried out on  $\text{Fe}_x\text{P}$ ,  $\text{Fe}_x\text{P}/\text{C}$ , and 20% Pt/C. It can be seen from Figure 4 that the radius of  $\text{Fe}_x\text{P}/\text{C}$  was smaller than the radius of  $\text{Fe}_x\text{P}$ , which indicates the  $\text{Fe}_x\text{P}/\text{C}$  had a smaller charge transfer resistance ( $R_{\text{ct}}$ ). The  $R_{\text{ct}}$  can be obtained by fitting the diameter of the quasi semi-circular arc in the medium- and high-frequency region on the Nyquist diagram, which is closely related to the charge transfer process at the interface of the electrode. The smaller the value is, the faster the reaction rate is. The  $R_{\text{ct}}$  value of  $\text{Fe}_x\text{P}/\text{C}$  ( $7.6 \Omega$ ) was significantly lower than  $\text{Fe}_x\text{P}$  ( $22.1 \Omega$ ), although it was still higher than that of Pt/C 20 wt% ( $4.7 \Omega$ ), indicating that the introduction of amorphous carbon materials by a high-temperature carbothermic reduction can accelerate the transfer of electrons/protons. Thus, the overall HER rate of the material was improved.

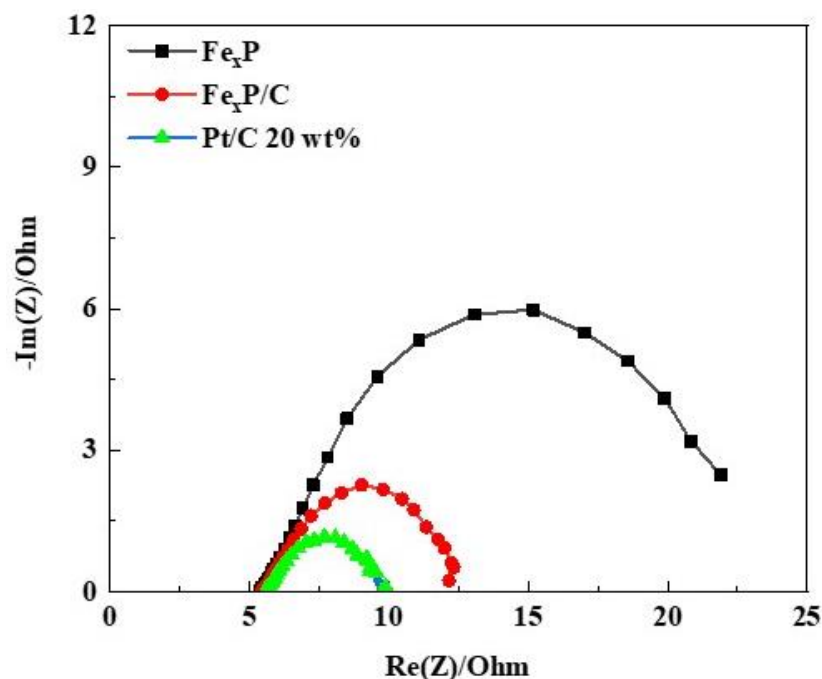


**Figure 4.** Nyquist plot for 20 wt% Pt/C, Fe<sub>x</sub>P, and Fe<sub>x</sub>P/C in 1 M KOH.

In addition to the important parameter of charge transfer impedance, the electrochemical active area (ECSA) and conversion frequency (TOF) of materials are also the key factors to reflect the essential electrochemical activity of materials [10,26]. The ECSA of the catalysts refers to the real effective area of the electrochemical reaction of the material. Cyclic voltammetry tests under different scanning rates were performed in the double-layer region, and the calculated double-layer capacitor ( $C_{dl}$ ) was used to study the ECSA. ECSA is directly proportional to the  $C_{dl}$ . Therefore, the greater the  $C_{dl}$  value is, the higher ECSA of the catalysts is. According to the CV results in Figure 5, Fe<sub>x</sub>P/C showed a larger CV area than Fe<sub>x</sub>P at the same sweep speed. In addition, the calculated  $C_{dl}$  of Fe<sub>x</sub>P/C ( $23.7 \text{ mF cm}^{-2}$ ) was larger and was more than two times that of Fe<sub>x</sub>P ( $10.7 \text{ mF cm}^{-2}$ ), which further indicates that the Fe<sub>x</sub>P/C had a larger ECSA and, on the surface of the Fe<sub>x</sub>P/C, more were provided.

Turnover frequency (TOF) is defined as the number of reactant molecules that can be converted into product molecules at an active site per unit time; the unit is  $\text{s}^{-1}$ . TOF is the essential property of catalysts; the higher the TOF value is, the higher the intrinsic catalytic activity of the catalysts is. The TOF values of the catalysts were calculated through the following equation [27]:

$$\text{TOF (s}^{-1}\text{)} = (j \times A) / (4 \times F \times n)$$

where the total number of hydrogen turnovers was calculated from the current density  $j$  applied at the overpotential of 150 mV for all catalysts,  $A$  is the geometric surface area of the electrode,  $F = 96,500 \text{ C mol}^{-1}$  and stands for the Faraday constant, and  $n$  (mol) is the mole number of the Fe metal(s) loaded on the GC electrode, which was determined by the ICP analysis. All Fe cations were assumed to be catalytically active; so, the calculated values represent the lower limits of the TOF. When the overpotential is 150 mV, the TOF value of Fe<sub>x</sub>P/C is  $0.15 \text{ s}^{-1}$ , which is twice that of Fe<sub>x</sub>P ( $0.07 \text{ s}^{-1}$ ). It also shows that the intrinsic HER activity of Fe<sub>x</sub>P/C is higher than that of Fe<sub>x</sub>P/C. Therefore, combined with a series of important parameters, such as the characteristic overpotential, Tafel slope, charge transfer impedance, electrochemically active area, and turnover frequency, the mixed crystal structure as well as the introduction of a carbon matrix can significantly improve the HER activity of Fe<sub>x</sub>P/C.

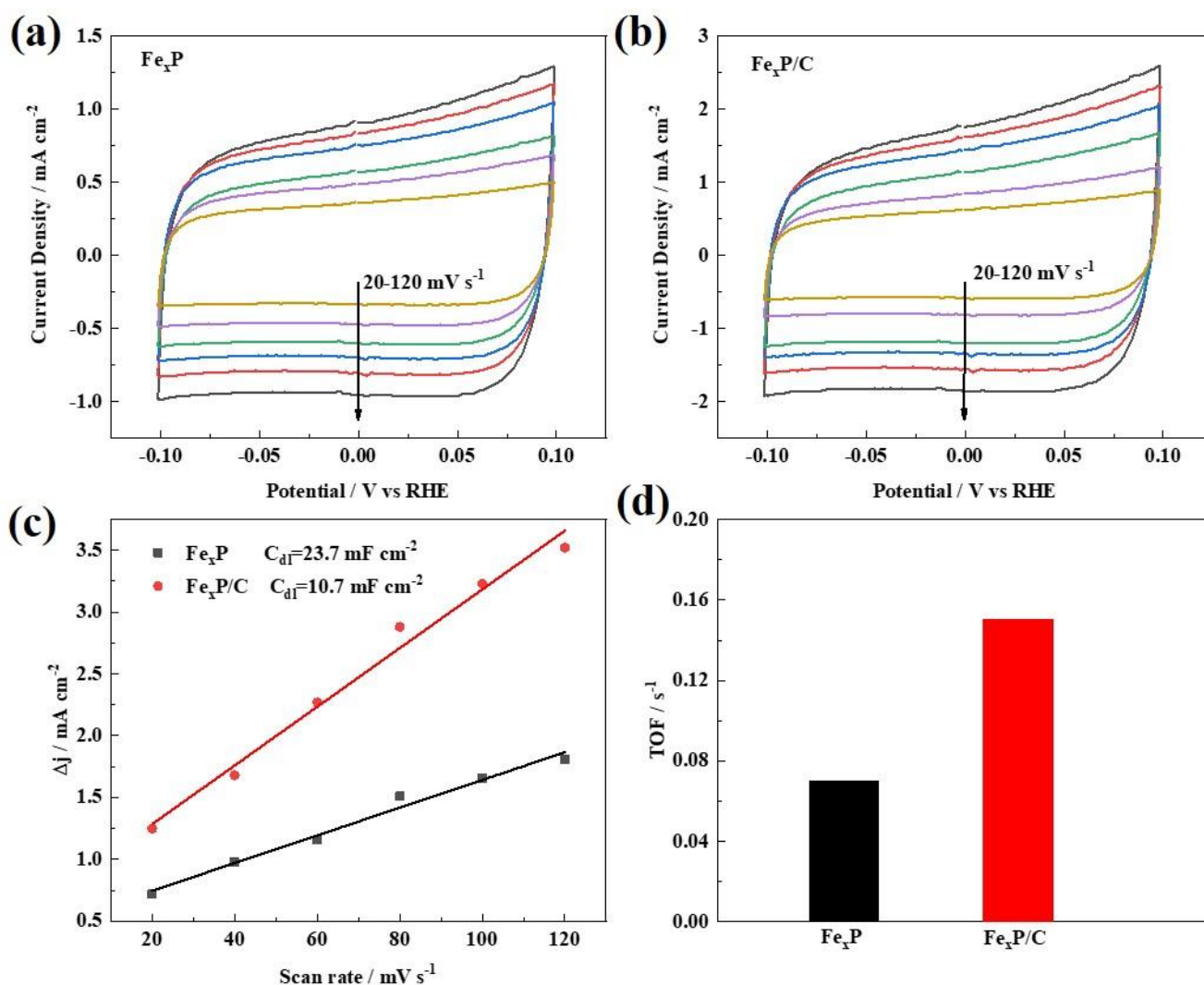


**Figure 5.** CV curves of (a) Fe<sub>x</sub>P and (b) Fe<sub>x</sub>P/C in non-Faradaic region at various scan rates; (c) CV current density versus scan rate plot; and (d) TOF plot for Fe<sub>x</sub>P and Fe<sub>x</sub>P/C under an overpotential of 150 mV.

Stability is also of great significance for catalysts, which can reflect the longtime working ability of catalysts in a certain environment [28,29]. In order to further study the electrocatalytic HER stability of the catalysts under acidic conditions, the cyclicality of the two materials was characterized. As shown in Figure 6, after 3000 CV cycles, the overpotential  $\eta_{10}$  of Fe<sub>x</sub>P/C only attenuated from the initial 221 mV to 226 mV and there was no obvious current loss, while the Fe<sub>x</sub>P material had worse stability and the overpotential  $\eta_{10}$  of Fe<sub>x</sub>P only attenuated from the initial 298 mV to 312 mV, which indicated that the introduction of a carbon matrix can increase the acid resistance of the active component Fe<sub>x</sub>P in the HER process.

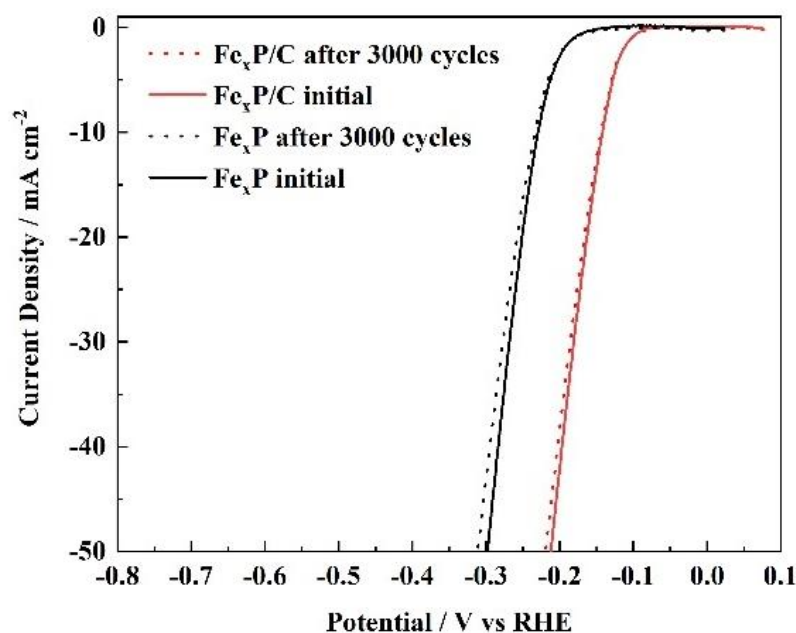


**Figure 6.** Comparison of the initial LSV curve (red, solid line) and the LSV curve after 3000 CV cycles (red, dashed line) for  $\text{Fe}_x\text{P}/\text{C}$ , and comparison of the initial LSV curve (black, solid line) and the LSV curve after 3000 CV cycles (black, dashed line) for  $\text{Fe}_x\text{P}$ .

#### 4. Conclusions

In this work, the industrial dephosphorization slags were firstly treated by acid leaching and precipitation. The mixture precipitation precursor was then gas–solid phosphated with sodium hypophosphite under low temperature (the produced catalyst was  $\text{Fe}_x\text{P}$ ) and carbothermally reduced under high temperature (the produced catalyst was  $\text{Fe}_x\text{P}/\text{C}$ ). The structure and composition of  $\text{Fe}_x\text{P}/\text{C}$  were characterized by XRD, SEM, EDS, and ICP. The electrochemical properties of the electrode were evaluated by CV, LSV, EIS, and cyclic stability. The results showed that the prepared  $\text{Fe}_x\text{P}/\text{C}$  was composed of  $\text{FeP}$ – $\text{Fe}_2\text{P}$  mixed nanocrystals supported on an amorphous carbon. In an alkaline medium, the corresponding overpotential when the output current density was  $10 \text{ mA cm}^{-2}$  ( $\eta_{10}$ ) was only 145 mV. Additionally, there was no obvious attenuation after 3000 cycles, which was significantly better than the electrocatalytic activity and stability of non-carbonaceous  $\text{Fe}_x\text{P}$  catalysts. A series of important parameters such as the characteristic overpotential, Tafel slope, charge transfer impedance, electrochemically active area and turnover frequency, the mixed crystal structure, and the introduction of a carbon matrix can significantly improve the HER activity of  $\text{Fe}_x\text{P}/\text{C}$ .

**Author Contributions:** Conceptualization, S.P. and L.L.; methodology, S.P.; software, Y.L.; validation, S.P., L.L. and S.H.; formal analysis, S.H.; investigation, S.P.; resources, Y.L.; data curation, S.P.; writing—original draft preparation, Y.L.; writing—review and editing, S.H.; visualization, S.H.; supervision, S.P.; project administration, L.L.; funding acquisition, L.L. All authors have read and agreed to the published version of the manuscript.

**Funding:** The research was financially sponsored by National Natural Science Foundation of China (Grant Nos. 51704080, 51874102, and 52074093).

**Conflicts of Interest:** The authors declare no conflict of interest.

#### References

1. Trinke, P.; Bensmann, B.; Hanke-Rauschenbach, R. Current density effect on hydrogen permeation in PEM water electrolyzers. *Int. J. Hydrog. Energy* **2017**, *42*, 14355–14366. [[CrossRef](#)]
2. Carmo, M.; Fritz, D.L.; Mergel, J.; Stolten, D. A comprehensive review on PEM water electrolysis. *Int. J. Hydrog. Energy* **2013**, *38*, 4901–4934. [[CrossRef](#)]

3. Li, L.; Wang, P.; Shao, Q.; Huang, X. Metallic nanostructures with low dimensionality for electrochemical water splitting. *Chem. Soc. Rev.* **2020**, *49*, 3072–3106. [[CrossRef](#)] [[PubMed](#)]
4. Liu, P.F.; Yin, H.; Fu, H.Q.; Zu, M.Y.; Yang, H.G.; Zhao, H. Activation strategies of water-splitting electrocatalysts. *J. Mater. Chem. A* **2020**, *8*, 10096–10129. [[CrossRef](#)]
5. Xiang, C.; Papadantonakis, K.M.; Lewis, N.S. Principles and implementations of electrolysis systems for water splitting. *Mater. Horiz.* **2016**, *3*, 169–173. [[CrossRef](#)]
6. Liu, W.; Zhang, H.; Li, C.; Wang, X.; Liu, J.; Zhang, X. Non-noble metal single-atom catalysts prepared by wet chemical method and their applications in electrochemical water splitting. *J. Energy Chem.* **2020**, *47*, 333–345. [[CrossRef](#)]
7. Zou, X.; Zhang, Y. Noble metal-free hydrogen evolution catalysts for water splitting. *Chem. Soc. Rev.* **2015**, *44*, 5148–5180. [[CrossRef](#)]
8. Xu, J.; Xiong, D.; Amorim, I.; Liu, L. Template-Free Synthesis of Hollow Iron Phosphide-Phosphate Composite Nanotubes for Use as Active and Stable Oxygen Evolution Electrocatalysts. *ACS Appl. Nano Mater.* **2018**, *1*, 617–624. [[CrossRef](#)]
9. Xu, J.; Li, J.; Xiong, D.; Zhang, B.; Liu, Y.; Wu, K.H.; Amorim, I.; Li, W.; Liu, L. Trends in activity for the oxygen evolution reaction on transition metal (M = Fe, Co, Ni) phosphide pre-catalysts. *Chem. Sci.* **2018**, *9*, 3470–3476. [[CrossRef](#)]
10. Anantharaj, S.; Ede, S.R.; Karthick, K.; Sankar, S.S.; Sangeetha, K.; Karthik, P.E.; Kundu, S. Precision and correctness in the evaluation of electrocatalytic water splitting: Revisiting activity parameters with a critical assessment. *Energy Environ. Sci.* **2018**, *11*, 744–771. [[CrossRef](#)]
11. Weng, C.C.; Ren, J.T.; Yuan, Z.Y. Transition Metal Phosphide-Based Materials for Efficient Electrochemical Hydrogen Evolution: A Critical Review. *ChemSusChem* **2020**, *13*, 3357–3375. [[CrossRef](#)] [[PubMed](#)]
12. Cao, S.; Wang, C.J.; Fu, W.F.; Chen, Y. Metal Phosphides as Co-Catalysts for Photocatalytic and Photoelectrocatalytic Water Splitting. *ChemSusChem* **2017**, *10*, 4306–4323. [[CrossRef](#)] [[PubMed](#)]
13. Callejas, J.F.; McEnaney, J.M.; Read, C.G.; Crompton, J.C.; Biacchi, A.J.; Popczun, E.J.; Gordon, T.R.; Lewis, N.S.; Schaak, R.E. Electrocatalytic and photocatalytic hydrogen production from acidic and neutral-pH aqueous solutions using iron phosphide nanoparticles. *ACS Nano* **2014**, *8*, 11101–11107. [[CrossRef](#)] [[PubMed](#)]
14. Kim, C.; Lee, S.; Kim, S.H.; Park, J.; Kim, S.; Kwon, S.H.; Bae, J.S.; Park, Y.S.; Kim, Y. Cobalt-Iron-Phosphate Hydrogen Evolution Reaction Electrocatalyst for Solar-Driven Alkaline Seawater Electrolyzer. *Nanomaterials* **2021**, *11*, 2989. [[CrossRef](#)]
15. Bonfant, G.; Balestri, D.; Perego, J.; Comotti, A.; Bracco, S.; Koepf, M.; Gennari, M.; Marchiò, L. Phosphine Oxide Porous Organic Polymers Incorporating Cobalt(II) Ions: Synthesis, Characterization, and Investigation of H<sub>2</sub> Production. *ACS Omega* **2022**, *7*, 6104–6112. [[CrossRef](#)] [[PubMed](#)]
16. Zhang, R.; Zhang, C.; Chen, W. FeP embedded in N, P dual-doped porous carbon nanosheets: An efficient and durable bifunctional catalyst for oxygen reduction and evolution reactions. *J. Mater. Chem. A* **2016**, *4*, 18723–18729. [[CrossRef](#)]
17. Kwong, W.L.; Gracia-Espino, E.; Lee, C.C.; Sandström, R.; Wågberg, T.; Messinger, J. Cationic Vacancy Defects in Iron Phosphide: A Promising Route toward Efficient and Stable Hydrogen Evolution by Electrochemical Water Splitting. *ChemSusChem* **2017**, *10*, 4544–4551. [[CrossRef](#)]
18. Yuan, Y.; Pei, H.; Chen, H.; Zuo, L.; Shen, J. Preparation of Fe<sub>2</sub>P and FeP catalysts for the hydrotreating reactions. *Catal. Commun.* **2017**, *100*, 202–205. [[CrossRef](#)]
19. Cho, G.; Park, Y.; Kang, H.; Hong, Y.K.; Lee, T.; Ha, D.H. Transition metal-doped FeP nanoparticles for hydrogen evolution reaction catalysis. *Appl. Surf. Sci.* **2020**, *510*, 145427. [[CrossRef](#)]
20. Wang, F.; Yang, X.; Dong, B.; Yu, X.; Xue, H.; Feng, L. A FeP powder electrocatalyst for the hydrogen evolution reaction. *Electrochem. Commun.* **2018**, *92*, 33–38. [[CrossRef](#)]
21. Zhang, X.Y.; Li, F.T.; Shi, Z.N.; Dong, B.; Dong, Y.W.; Wu, Z.X.; Wang, L.; Liu, C.G.; Chai, Y.M. Vanadium doped FeP nanoflower with optimized electronic structure for efficient hydrogen evolution. *J. Colloid Interface Sci.* **2022**, *615*, 445–455. [[CrossRef](#)] [[PubMed](#)]
22. Deng, Y.; Xi, X.; Xia, Y.; Cao, Y.; Xue, S.; Wan, S.; Dong, A.; Yang, D. 2D FeP Nanoframe Superlattices via Space-Confined Topochemical Transformation. *Adv. Mater.* **2022**, *34*, 2109145. [[CrossRef](#)] [[PubMed](#)]
23. Zheng, S.; Yu, T.; Lin, J.; Lou, H.; Xu, H.; Yang, G. FeP<sub>3</sub> monolayer as a high-efficiency catalyst for hydrogen evolution reaction. *J. Mater. Chem. A* **2019**, *7*, 25665–25671. [[CrossRef](#)]
24. Ling, T.; Yan, D.Y.; Wang, H.; Jiao, Y.; Hu, Z.; Zheng, Y.; Zheng, L.; Mao, J.; Liu, H.; Du, X.W.; et al. Activating cobalt(II) oxide nanorods for efficient electrocatalysis by strain engineering. *Nat. Commun.* **2017**, *8*, 1509. [[CrossRef](#)]
25. Štrbac, S.; Smiljanić, M.; Wakelin, T.; Potočnik, J.; Rakočević, Z. Hydrogen evolution reaction on bimetallic Ir/Pt(poly) electrodes in alkaline solution. *Electrochim. Acta* **2019**, *306*, 18–27. [[CrossRef](#)]
26. McEnaney, J.M.; Crompton, J.C.; Callejas, J.F.; Popczun, E.J.; Read, C.G.; Lewis, N.S.; Schaak, R.E. Electrocatalytic hydrogen evolution using amorphous tungsten phosphide nanoparticles. *Chem. Commun.* **2014**, *50*, 11026–11028. [[CrossRef](#)]
27. Yao, Y.; Mahmood, N.; Pan, L.; Shen, G.; Zhang, R.; Gao, R.; Aleem, F.E.; Yuan, X.; Zhang, X.; Zou, J.J. Iron phosphide encapsulated in P-doped graphitic carbon as efficient and stable electrocatalyst for hydrogen and oxygen evolution reactions. *Nanoscale* **2018**, *10*, 21327–21334. [[CrossRef](#)]

28. Wang, H.; Wang, X.; Zheng, B.; Yang, D.; Zhang, W.; Chen, Y. Self-assembled Ni<sub>2</sub>P/FeP heterostructural nanoparticles embedded in N-doped graphene nanosheets as highly efficient and stable multifunctional electrocatalyst for water splitting. *Electrochim. Acta* **2019**, *318*, 449–459. [[CrossRef](#)]
29. Huang, G.; Zhang, C.; Liu, Z.; Yuan, S.; Yang, G.; Wang, K.; Li, X.; Li, N.; Jing, S. Self-Supported Mesoporous Iron Phosphide with High Active-Site Density for Electrocatalytic Hydrogen Evolution in Acidic and Alkaline Media. *ChemElectroChem* **2020**, *7*, 4943–4948. [[CrossRef](#)]